1  **Title:** Dynamical links between small- and large-scale mantle heterogeneity:
2  seismological evidence
3

4  **Authors:** Daniel A. Frost[1]*, Edward J. Garnero[2], and Sebastian Rost[3]

5

6  **Affiliations:**

7  [1]Earth & Planetary Science, University of California, Berkeley, California, USA

8

9  [2]School of Earth and Space Exploration, Arizona State University, Tempe, Arizona,

10  USA

11

12  [3]Institute of Geophysics and Tectonics, School of Earth and Environment, University

13  of Leeds, Leeds, UK

14

15  *Correspondence to: dafrost@berkeley.edu

16  **Abstract**
17
18  We identify PKP•PKP scattered waves (also known as P′•P′) from earthquakes

19  recorded at small-aperture seismic arrays at distances less than 65°.  P′•P′ energy

20  travels as a PKP wave through the core, up into the mantle, then scatters back down

21  through the core to the receiver as a second PKP. P′•P′ waves are unique in that they

22  allow scattering heterogeneities throughout the mantle to be imaged. We use array-

23  processing methods to amplify low amplitude, coherent scattered energy signals

24  and resolve their incoming direction. We deterministically map scattering

25  heterogeneity locations from the core-mantle boundary to the surface. We use an

extensive dataset with sensitivity to a large volume of the mantle and a location method allowing us to resolve and map more heterogeneities than have previously been possible, representing a significant increase in our understanding of small-scale structure within the mantle. Our results demonstrate that the distribution of scattering heterogeneities varies both radially and laterally. Scattering is most abundant in the uppermost and lowermost mantle, and a minimum in the mid-mantle, resembling the radial distribution of tomographically derived whole-mantle velocity heterogeneity. We investigate the spatial correlation of scattering heterogeneities with large-scale tomographic velocities, lateral velocity gradients, the locations of deep-seated hotspots and subducted slabs. In the lowermost 1500 km of the mantle, small-scale heterogeneities correlate with regions of low seismic velocity, high lateral seismic gradient, and proximity to hotspots. In the upper 1000 km of the mantle there is no significant correlation between scattering heterogeneity location and subducted slabs. Between 600 and 900 km depth, scattering heterogeneities are more common in the regions most remote from slabs, and close to hotspots. Scattering heterogeneities show an affinity for regions close to slabs within the upper 200 km of the mantle. The similarity between the distribution of large-scale and small-scale mantle structures suggests a dynamic connection across scales, whereby mantle heterogeneities of all sizes may be directed in similar ways by large-scale convective currents.

## 1. Introduction

50        The high frequency (~1 Hz) seismic wavefield provides evidence of

51        kilometre scale structure within the Earth [Cleary and Haddon, 1972]. Seismic

52        energy that is not explained by wave propagation in smoothly varying velocity

53        models of the Earth has been attributed to reflections and scattering from sharply

54        contrasting volumetric heterogeneities and roughness on interfaces [Chang and

55        Cleary, 1981]. The interaction of the wavefield with discrete, small-scale variations

56        in elastic properties and/or density can divert seismic energy onto new paths, often

57        generating precursors or postcursors (coda) to the main seismic phases that travel

58        in the great circle plane. The size of the scatterers that can be imaged is dependent

59        upon the wavelength that is analysed; for the teleseismic high-frequency P-

60        wavefield above 1 Hz they are typically on the order of 1 to 10 km.

61        Global imaging of Earth's small-scale heterogeneities is difficult due to the

62        uneven distribution of earthquake sources and seismic receivers, and the low

63        amplitude of the scattered signals involved. Scattering can be studied using single

64        stations, but with this approach the location of the scattering heterogeneity can be

65        ambiguous [Wen, 2000]. Alternatively, seismic arrays, i.e., 3 or more closely located

66        sensors, can resolve the incoming direction of scattered waves, thus it is possible to

67        deterministically locate heterogeneities [Thomas et al., 1999; Rost and Earle, 2010;

68        Frost et al., 2013]. In the last few decades a number of studies have started to

69        unravel the distribution of small-scale heterogeneities of Earth's mantle. Hedlin et al.

70        [1997], and later Mancinelli and Shearer [2013, 2016] studied the depth

71        distribution of heterogeneity within the mantle through analysis of PKP pre- and

72        postcursors recorded at single stations. Using a stochastic Rayleigh-Born scattering

73    approach, Mancinelli and Shearer [2013, 2016] developed a global model of

74    scattering heterogeneity containing 0.1% root-mean-square velocity variations in

75    the deepest 1200 km of the mantle with heterogeneity scale sizes ranging from 2 to

76    30 km.

77          This work is complemented by studies that deterministically map small-scale

78    scattering heterogeneity within the upper and lower mantle. These studies have

79    noted lateral variations in heterogeneity distribution, as well as variations in

80    amplitudes of scattered waves. Scattered P-to-P (P•P, where the "•" represents the

81    location of scattering) and P-to-S (P•S) waves are sensitive to heterogeneities in the

82    upper half of Earth's mantle; they have been used to map scattering heterogeneity in

83    regions influenced by recent subduction [Kaneshima and Helffrich, 1998; Bentham

84    and Rost, 2014]. Scattering in the lowermost mantle has also been observed to vary

85    laterally [Waszek et al., 2015]. Strong scattering has been observed in regions

86    beneath mantle hotspots [Wen, 2000], near small, regional ultra-low velocity zone

87    (ULVZ) structures [Yao and Wen, 2014], beneath subduction zones [Miller and Niu,

88    2008], and near the edges of LLSVPs [Frost et al., 2013]. A near-global study of

89    PK•KP – a PKP wave that is back-scattered in the lower mantle onto a second PKP

90    path – suggests a spatial correlation between scattering and LLSVP edges in the

91    lowermost 300 km of the mantle [Rost and Earle, 2010; Frost et al., 2017].

92          The volume of the mantle that can be investigated for scattering

93    heterogeneity is controlled by the specifics of the seismic probe. PK•KP can be used

94    to investigate the lower mantle close to the CMB [Chang and Cleary, 1981; Rost and

95    Earle, 2010; Frost et al., 2017]. The direct wave PKPPKP (also called P′P′) results

96   from a PKP wave (P′) reflecting from the underside of the surface, back into the

97   Earth as a second PKP wave, along the great-circle path (GCP). This phase can be

98   preceded by scattered energy called PKP•PKP (P′•P′), caused by back-scattering of

99   PKP at any depth in the mantle [Rost et al., 2015]. Like PK•KP, P′•P′ has an unusual

100  scattering geometry (Fig. 1) and can scatter from locations off the GCP, and the P′

101  segments need not be symmetric to each other. P′•P′ is the continuation of PK•KP

102  towards the surface, thus this phase is able to sample the whole mantle from CMB to

103  crust (Fig. 2). We extend our earlier work and investigate the mantle upwards from

104  the CMB to the surface to deterministically map the vertical and lateral distribution

105  of scattering heterogeneities throughout the mantle.  In contrast to other scattering

106  probes, the unusual (and versatile) raypath geometry of P′•P′ allows the study of

107  previously unsampled regions of the Earth.

108       The internal structure of the Earth and the nature of mantle convection are

109  inherently connected across scales [e.g. Tackley 2015]. The distribution of large-

110  scale mantle structure as imaged by seismic tomography has been investigated

111  using thermo-chemical geodynamic models, which indicate that downwelling of cold,

112  dense slabs at subduction zones moves and shapes the hot, convecting piles of

113  seismically slow material at the CMB, forming the Large Low Shear Velocity

114  Provinces (LLSVPs) [McNamara and Zhong, 2005; Li et al., 2014; Domeier et al,

115  2016]. The LLSVPs, if compositionally distinct, may modulate mantle dynamics

116  through thermal instabilities that result in mantle plumes that rise up causing

117  hotspot volcanism [Thorne et al., 2004; French and Romanowicz, 2015].

118  Furthermore, calculations suggest that mantle plumes may be spatially correlated

119    with the LLSVPs [Thorne et al., 2004; Doubrovine et al., 2016]. Geodynamic

120    modelling of thermo-chemical structures in the deep mantle indicates that small-

121    scale heterogeneities (as small as kilometre-sized) can be passively transported in

122    the large-scale flow [Brandenburg and van Keken, 2007; Li et al., 2014, Mulyukova

123    et al., 2015]. Furthermore, geochemical analysis of intraplate volcanism suggests

124    that heterogeneities situated in the deep Earth may be transported to the surface by

125    entrainment in mantle convection [Williams et al., 2015]. Therefore, there is

126    compelling evidence that the distribution of small-scale seismic structure in the

127    mantle is linked to the large-scale structures.

128        Here we use a global collection of earthquakes recorded at seismic arrays to

129    identify P′•P′ and deterministically locate the position of the causative volumetric

130    scattering heterogeneity within the mantle. We investigate the relationship between

131    scattering heterogeneity and other seismologically imaged structures in the mantle.

132    We use our observations to understand the distribution of small-scale

133    heterogeneities throughout the whole of the mantle, and the connection with

134    dynamic processes.
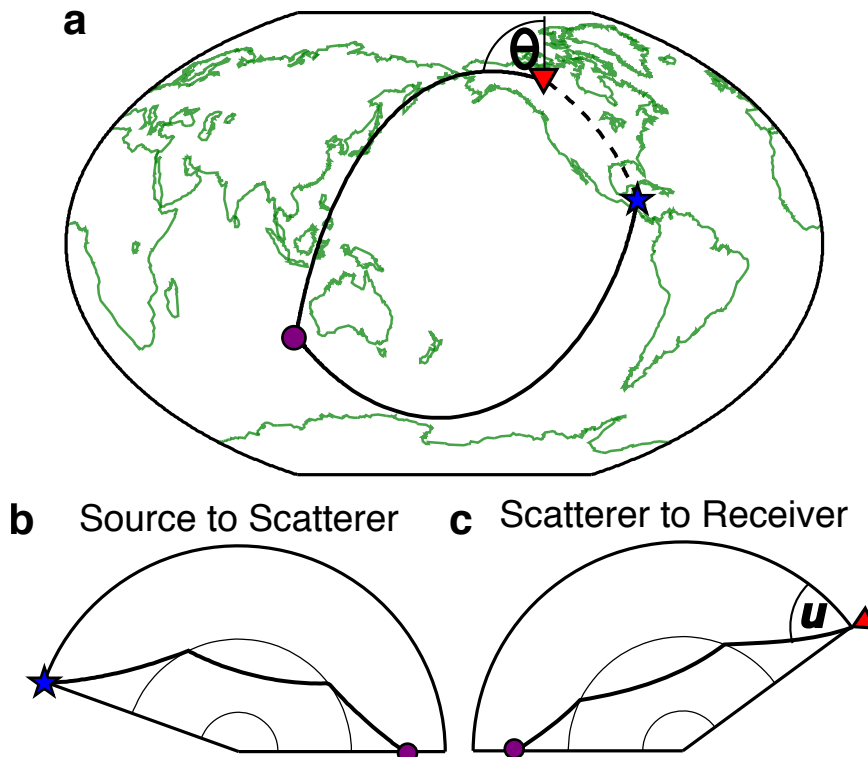
**Figure 1:** PKP•PKP (P′•P′) example path. **(a)** A P′•P′ path from the source (star) to a scattering point in the mantle (circle) and then to the receiver (triangle). P′•P′ travels along two great-circle paths (solid lines) to and from the scattering point, off the great-circle path between the source and receiver (dashed line). PKP ray paths from **(b)** source to scatterer (PKP$_{ab}$) and **(c)** scatterer to receiver (PKP$_{bc}$). The two PKP legs may be symmetric or asymmetric (as in this case) and can scatter from any depth in the mantle from the CMB to the surface. Rays observed at the surface arrive from a specific direction known as the back-azimuth, $\theta$, measured relative to North, or the relative back-azimuth measured from the GCP, and from a vertical incidence angle, referred to as the slowness, $u$.

[SINGLE OR 1.5 COLUMN FIGURE]
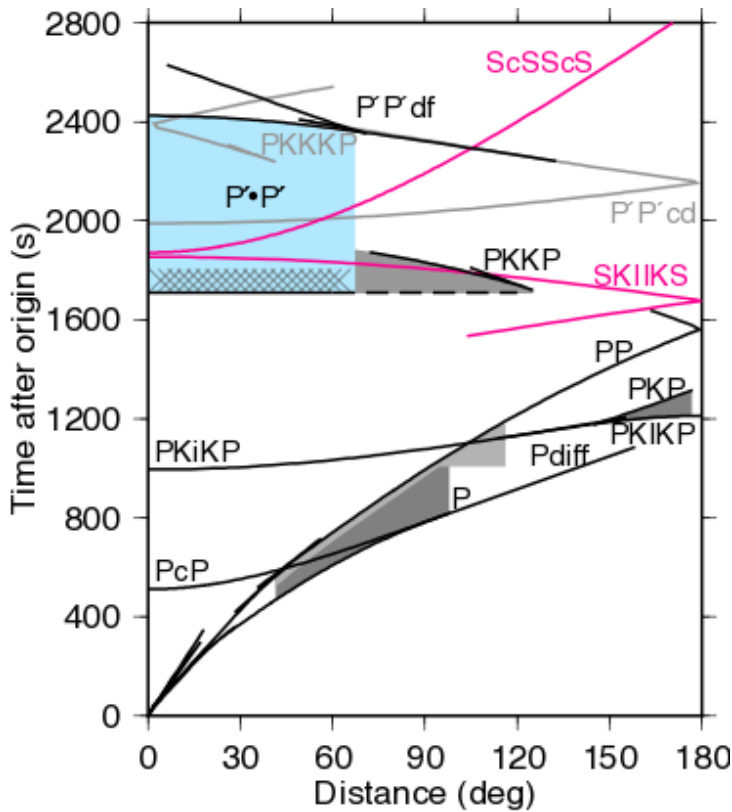
**Figure 2:** Travel-time curve displaying P′•P′ and other scattered phases in the high-frequency seismic wavefield. Black lines mark major P-wave phases. The blue region marks the time and distance region investigated for P′•P′ waves in this study. Hatched region marks time and distance region investigated for PK•KP in Frost et al., [2017]. Grey and pink lines mark the P- and S-waves, respectively, that may contaminate the P′•P′ study region. Other P- and S-waves are not shown for clarity. Differently shaded grey regions denote time and distance regions previously investigated for other scattered waves. Adapted from Rost et al., [2015].

[SINGLE COLUMN FIGURE]

## 2. Data

We collect data from 643 earthquakes at any depth with magnitudes M≥6 recorded at up to 12 small and medium aperture arrays within 65° of any event (Fig. 3). The arrays contain a mixture of short period and broadband instruments; we use only the most common instrument type in each array. These arrays were designed

169    to determine the directivity of short-period P-waves thus are ideally suited for

170    analysis of high-frequency scattered waves. The aperture of an array controls its

171    directivity resolution, thus we select only arrays with apertures of 10km to 30 km to

172    ensure that we are able to resolve well the incoming direction of waves.

173          Each event-array pair has a specific geographical volume of the mantle from

174    which possible P′•P′ scattered waves can be detected (Fig. 3). The size and shape of

175    the sampling region at any given scattering depth is dependent on the event-array

176    distance. Using estimations of the potential scattering volumes combined for all

177    source-array pairs, we develop a "potential sampling density map" of our dataset for

178    different depths, which represents the abundance of scatterers we would detect if

179    the actual distribution of scattering in the Earth distribution were uniform. The

180    potential scatterer sampling distribution of the dataset is uneven, but in contrast to

181    other probes, the southern hemisphere is well covered throughout the depth of the

182    mantle, allowing investigation of the relationship between scattering

183    heterogeneities and the South and Central American subduction zones, and the

184    African and Pacific LLSVPs.
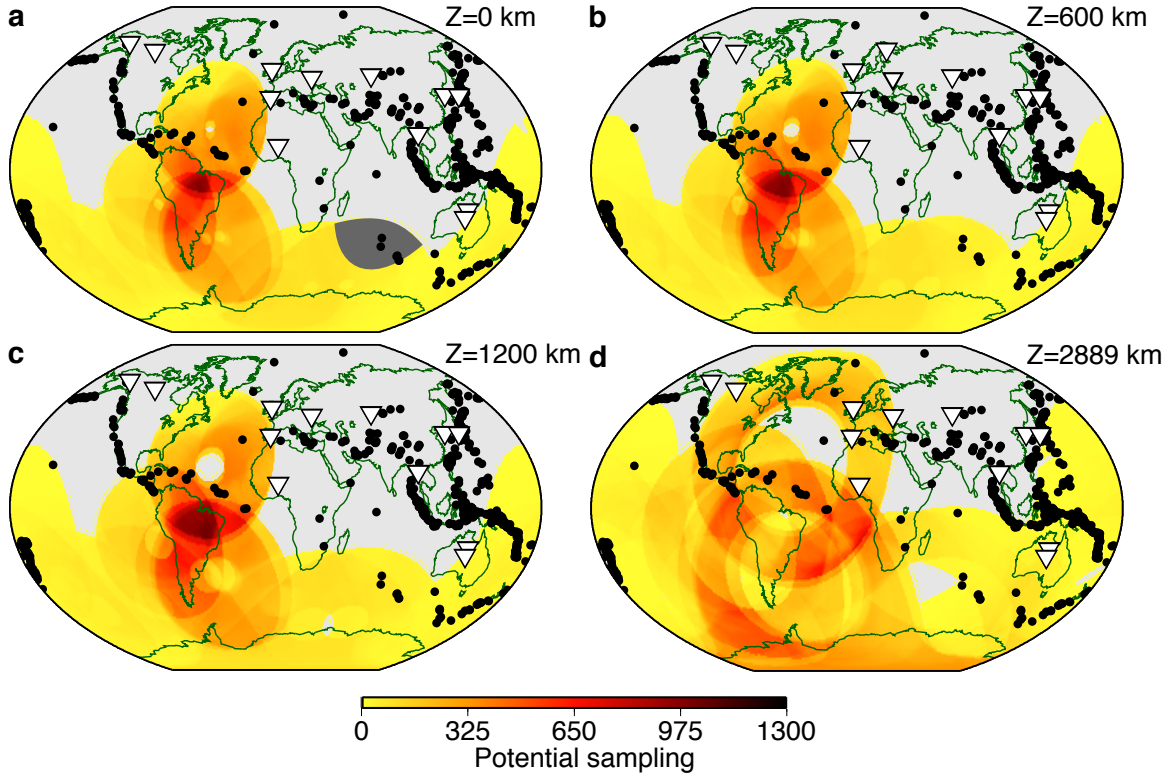
**Figure 3:** Earthquakes (dots) and arrays (triangles) in our dataset and resultant potential P′•P′ scattering sampling. The 643 events and up to 12 arrays yielded 1715 event-array pairs. Global sampling distributions are constructed by summation of the potential scattering sampling for all source-array pairs at: **(a)** the surface (0 km depth); **(b)** transition zone (600 km depth); **(c)** mid-mantle (1200 km depth); and **(d)** the Core-Mantle Boundary (2889 km depth). Sampling is densest in the mid-mantle and most geographically extensive in the lowermost mantle. Grey wedge in **(a)** displays an example of the potential scattering regions for a single event-array pair.

[2 COLUMN FIGURE]


## 3. Methods

We investigate energy associated with mantle scattering in a time window from the first possible arrival of P′•P′ at ~1700s after the earthquake origin time (for a surface focus event) corresponding to scattering at the CMB, up to the first

203    possible arrival of the direct wave  $P' \bullet P'_{df}$ at ~2400s, which is the earliest $P' \bullet P'$ GCP

204    phase, reflecting from the underside of the surface on the antipodal side (Fig. 2).

205    $P' \bullet P'$ scattering related to interactions with small-scale mantle heterogeneity is

206    feasible for any time and distance in this window (blue shaded region in Fig. 2).

207         We de-trend the data and discard any discontinuous traces i.e. gaps in the

208    recording. The remaining traces are filtered with a $2^{nd}$ order bandpass between 0.5

209    and 2 Hz to enhance the frequencies most associated with small-scale scattering in

210    past studies that investigated frequency content [Mancinelli et al., 2016; Frost et al.,

211    2017].  We search for scattered signals within the wavefield data using fk-analysis

212    (frequency-wavenumber), which performs a grid-search over incoming directions

213    to maximise coherence (the similarity of two or more signals in the frequency

214    domain) of the signal stacked across the array, calculated in the frequency domain

215    [Capon, et al., 1967]. We search over slownesses from 0 to 8 sec/deg and back-

216    azimuths between -180° to 180° relative to the GCP. By selecting signals with the

217    highest coherence we determine the best fitting slowness vector (a combination of

218    the back-azimuth, $\theta$, and the horizontal slowness, $\underline{u}$) of the incoming signals in the

219    scattering search time-window (1700s to 2400s after earthquake origin). To

220    improve the resolution of the slowness vector of incoming signals, as well as to

221    further increase the prominence of signals above the noise, we apply the F-statistic

222    to the fk-analysis (Fig. 4) [Blandford, 1974; Selby, 2011]. The F-statistic calculates

223    the ratio of the amplitude of the stacked signal to the sum of the differences between

224    the stack and each trace used to form the stack. The F-trace has the effect of

225    penalising stacks that differ from individual input traces i.e. signals that are

226     incoherent across the array. Thus, the best fitting slowness and back-azimuth from

227     the grid-search are those that produce the most representative stack of the

228     individual array traces. By performing these calculations in the frequency domain

229     we increase efficiency by reducing the number of transformations required between

230     the time and frequency domains. However, the fk approach returns a single value of

231     coherence from each slowness vector averaged across the whole time window, thus

232     collapsing the time axis. Combining the F-statistic with traditional fk-analysis results

233     in much-improved slowness vector resolution, even for the small-aperture arrays

234     used here [Frost et al., 2013]. Thus the origin of the scattered energy can be more

235     precisely estimated.

236         We measure the slowness and back-azimuth of the most coherent signals

237     received at the array in consecutive 50 s long time windows (Fig. 4). This window

238     length gives depth resolution comparable to that obtained in global tomography

239     models, and is sufficient to identify broad-scale trends in scattering distribution,

240     both laterally and with depth. We assume the arrival time of a signal to be the

241     middle of the 50 s time window, and given that scattering of P′•P′ from a range of

242     depths can arrive at the array with similar travel-times, each 50 s time window that

243     we investigate is sensitive to scattering from a 50 to 200 km thickness of the mantle.

244     The thickness of the scattering region that each time window is sensitive to

245     decreases with scattering depth hence, at shallower depths, there is overlap in

246     depth sensitivity between windows – adjacent time windows can contain energy

247     scattered from the same depth (albeit from different locations).

248    Mantle scattered P′•P′ waves are expected to arrive with slownesses

249    between 2.1 and 4.4 s/deg. The range of directions from which P′•P′ waves can be

250    observed is dependent upon the event-array distance and scattering depth. Array

251    analyses permit recognition and omission of contaminating waves by determination

252    of the incoming direction of energy, compared with the directions possible for P′•P′.

253    We compute the expected arrival times for possible contaminating waves: direct

254    phases, depth phases, and multiple reflections of both P- and S-waves. We do not

255    calculate multiples reflecting off upper mantle discontinuities (i.e. a downgoing

256    wave reflecting off the 660 km discontinuity, then reflecting back down from the

257    410 km discontinuity).  Contaminating waves would likely be detected along the

258    GCP (we take both minor and major arc arrivals into account). In contrast, P′•P′

259    scattered energy most commonly arrives off the GCP, allowing clear identification of

260    the scattered arrivals. However, at short event-array distances it is possible for P′•P′

261    to arrive along the GCP; these situations can be predicted and extra care is taken to

262    exclude contaminating phases. As there are few phases that can arrive within the

263    P′•P′ window (Fig 2), we would expect few time windows to be contaminated by

264    other seismic phases. Nonetheless, we discard any time window where we both

265    observe a signal within 20 degrees of the GCP (in major or minor arc directions) and

266    any known seismic wave is predicted to arrive in the same time window and along

267    the same backazimuth (i.e. minor or major great-circle path) (e.g Fig. 4d).  Of all

268    identified signals, only 2% match the time and direction predicted for known

269    seismic phases, and thus are discarded.

270    The wavefield may also be contaminated by foreshocks or aftershocks to the

271    analysed events, thus we exclude from further analysis any scattered signals where

272    any magnitude ≥6 earthquake occurs within two hours of the origin time of the

273    studied earthquake (11% of identified scattered signals). As a further test we

274    remove any scattered signal that could be contaminated by a magnitude ≥5 event

275    but find no systematic difference in the distribution of scattering heterogeneity. Our

276    focus on core wave arrivals with slownesses from 2.1 to 4.4 s/deg helps to exclude

277    contamination from smaller, closer events, which have higher slownesses associated

278    with more horizontal incoming energy (and the discarding of GCP signals further

279    minimizes energy from small local events contributing to data we analyse).

280    Therefore, we are certain that our data selection prevents any contamination of the

281    results by local and regional events. Lithospheric scattering directly beneath the

282    array may redirect high slowness contaminating energy to lower slownesses typical

283    of mantle scattering that we consider here. However, the direct contaminating wave

284    would arrive in the same time window as the lithospheric scattered energy, and

285    would likely be more coherent with an obviously inappropriate slowness.  This

286    allows a straightforward identification (and removal) of energy scattered from

287    lithospheric structure.

288    After contaminated time windows have been removed, scattered signals are

289    identified. We pick time windows containing energy prominently above the

290    background noise level in f-k space and consistent with the directivity criteria for

291    P′•P′ scattering (e.g. Fig. 4b). We identify the slowness and back-azimuth of the

292    scattered signal, and select the time at the middle of the 50 s long window as

293  scattered travel time; therefore, we only identify one scattered signal per 50 s

294  window. If multiple P′•P′ signals are observed in the same time window we retain

295  the signal with the highest coherence, as this will be the best spatially resolved.

296  Multiple waves arriving at a similar time, either scattered or direct, may interfere

297  causing the apparent arrival direction of energy at the array to be incorrect. The

298  apparent signal would likely appear blurred across directions, thus we only select

299  signals with tightly resolved slowness and back-azimuth (within the capabilities of

300  the array).

301        The back-azimuth, slowness, and time information for each scattered signal

302  are used to calculate a scattering location in the mantle. The back-azimuth of a

303  signal indicates the horizontal direction along which the wave travelled while the

304  slowness defines a discrete path for a 1D Earth model, and the travel-time relates to

305  the scattering depth (Fig. S1). Thus there is a trade-off between the distance and

306  depth of a scattered path, hence we attempt to fit both slowness and travel-time

307  simultaneously with a grid search. We ray trace backwards from the array along the

308  observed back-azimuth to a range of possible scattering depths and distances, and

309  then ray-trace from these scattering locations to the source. Possible scattering

310  locations are spaced every 0.01° in distance between the minimum and maximum

311  possible path lengths of PKP along the resolved back-azimuth and 50 km in depth

312  from the CMB to the surface. We model the scattering location by minimising the

313  misfit between the calculated slowness and time for each potential scattering

314  location and the observed values. Mapped scattering heterogeneity locations are

315  discarded if traced rays to the solution location do not well fit the observed

316    slowness and time: if the squared slowness misfit (observed minus predicted) plus

317    twice the squared time misfit is greater than 10, i.e. a weighting factor of 2 is used

318    for travel time misfit and therefore we favour fitting scattering locations with small

319    travel-time misfits. The misfit value selected fits signals within the slowness

320    resolution limit of the arrays. Overall, of the original 4319 identified scattered

321    signals, we discard signals contaminated by other events (11% of the original

322    population), other phases (2%), and poorly fit signals (44%), leaving 1876 mapped

323    scattering heterogeneities.

324         Due to the uncertainty in travel-time (from using the middle of the 50 s time

325    window) and the uncertainty in slowness (due to the ability of the arrays to resolve

326    the incoming direction) we determine the dimensions of the region that contains the

327    heterogeneity based on these limitations. We calculate scattering locations for

328    signals arriving at the start and end of the 50s time window, and with slowness

329    variation of ±0.3 s/deg relative to that measured at the array (estimated from the

330    slowness spacing of the grid-search). This defines a region around the best fitting

331    heterogeneity location that is, on average, ±100 km laterally and vertically. For mid-

332    mantle scattering at high slowness values (~1000-1800 km depth), the error

333    regions can occasionally grow to values as large as ±800 km laterally and ±500 km

334    vertically but this larger misfit is only relevant for around 5% of the solution

335    scattering locations, thus the majority of the scattering heterogeneities identified in

336    our dataset are located to within ±100 km vertically and laterally.

337         Sub-surface structure beneath the majority of the arrays used in this study

338    has been demonstrated to have an insignificant effect on the resolved slowness and

339    back-azimuth (Bondar et al., 1999). Nevertheless, removing scattering

340    heterogeneities observed at Chiang Mai array, which is most affected by sub-surface

341    structure, dominantly reduces scattering in the upper 200 km of the mantle and

342    causes no significant change in our conclusions on the relationship with lower

343    mantle structure.

344

345
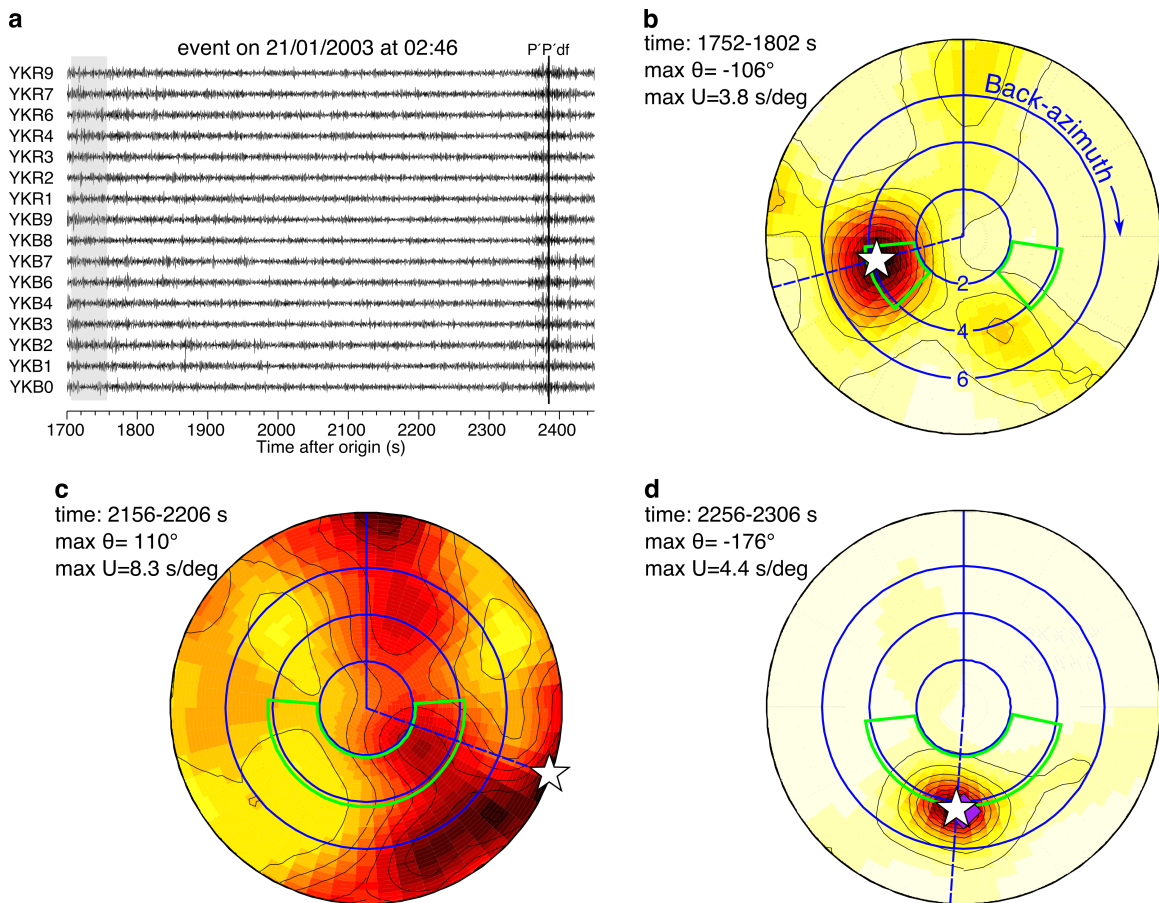


346
347    **Figure 4:** Array data are shown for (**a** and **b**) a magnitude 6.5 event, 24 km depth,

348    52° away from Yellowknife array, and (**c** and **d**) a magnitude 7.8 event, 0 km depth,

349    37° away from Warramunga array. **(a)** The time window for P′•P′ scattering (1700-

350    2450 sec for this event, blue region in Fig. 2). The predicted time of the direct phase,

351    P′P′$_{df}$, is shown by the vertical line, marking the end of the scattering window used

352    here. Data are filtered between 0.5 and 2.0 Hz. The grey shaded time window

353 corresponds to information shown in **(b)**. **(b)** f-k processing of the 50 sec time

354 window shown grey in **(a)**, displayed in terms of back-azimuth ( $\theta$ , azimuthal axis)

355 and slowness (*u*, radial axis outwards from 0 to 8 s/deg with rings marking 2 to 6

356 s/deg). Back-azimuth is measured relative to the great-circle path (vertical blue

357 line). The white star shows the maximum coherence in the f-k analysis, arriving with

358 relative back azimuth = -106° (blue dashed line).  The 90% coherence contour is

359 roughly ±10° wide in back-azimuth and ±0.5 s/deg in slowness around the

360 maximum. The green regions show the range of possible slownesses and back-

361 azimuths for P′•P′ waves scattering at this distance and the median depth of

362 scattering for this time window (from the shape of the potential scattering regions,

363 grey regions in Fig. 3). **(c)** f-k processing of a time window showing no clear P′•P′

364 waves. (**d**) f-k processing of a time window that is likely contaminated by the direct

365 phase PKKKP (predicted slowness and back-azimuth marked by purple diamond).

366 Time windows (**c**) and (**d**) are not picked for further processing.

367 [2 COLUMN FIGURE]

368
369
370
371 **4. Results**
372
373 The mapped locations of scattering heterogeneities are unevenly distributed

374 in the mantle, both laterally and with depth. This is not unexpected given that the

375 potential sampling capacity of our dataset also varies in location and depth (Fig. 3).

376 We divide the number of mapped scatterers by the potential sampling density (Fig.

377 3) in order to compare relative scattering density for different regions. This

378 normalised scattering population shows that heterogeneities are distributed

379 throughout the mantle, but more abundant scattering heterogeneity is present in

380 the uppermost and lowermost mantle (Fig. 5). The radial scatterer distribution also

381 shows a small increase in scattering heterogeneity between 600 and 900 km depth,

382    just below the transition zone, and a minimum in the mid-mantle between 1400 to

383    1800 km depth.

384          We find that the radial abundance of small-scale scattering heterogeneity

385    matches the RMS amplitude of large-scale tomographic velocities (Fig. 5): scattering

386    is most common and the RMS variation of tomographic velocities is highest in the

387    uppermost and lowermost mantle. This correlation holds roughly for all

388    tomographic models (Fig. S2).

389
390



391
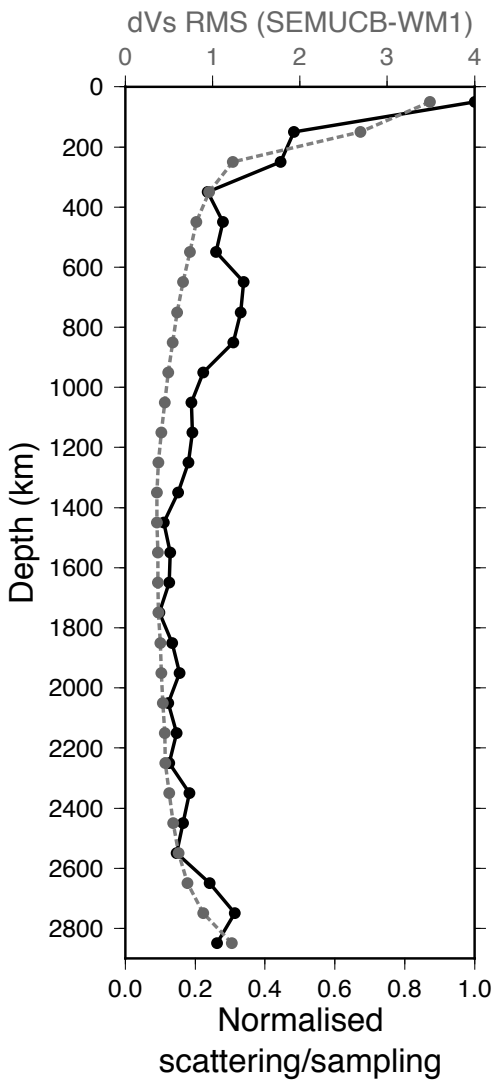
392   **Figure 5:** Normalised scattering heterogeneity density with depth (number of

393   scatterers divided by number of samples in each 100 km thick layer) for the

394   complete dataset (black, lower x-axis) and RMS of the shear velocity perturbations

395   from the global tomographic model SEMUCB-WM1 (grey and dashed, upper x-axis)

396   [French and Romanowicz, 2014]. The depth distribution of small-scale scattering

397   heterogeneity roughly correlates with the RMS of long-wavelength dVs

398   perturbations. Both lines are scaled to fit the same axis.

399   [SINGLE COLUMN FIGURE]

400
401
402        We investigate possible spatial correlation between the resolved scattering

403   heterogeneities and large-scale mantle features, which may be interpreted as

404   proxies for dynamic processes, as in Frost et al., [2017]. We compare the location of

405   scattering heterogeneity to geographical regions beneath hotspots, subducted slabs,

406   regions of high and low tomographic velocities, and regions of high and low lateral

407   tomographic velocity gradients. The high/low velocities and gradients from

408   tomographic models likely relate to the locations of LLSVPs and subducted slabs in

409   the mantle.   The spatial locations of scattering heterogeneities are shown,

410   normalised by sampling, in the Supplementary Material, while the absolute latitude,

411   longitude, and depth information for each scattering heterogeneity is shown in

412   Supplementary Table 1

413

414

415   *4.1 Relationship between scattering heterogeneities and mantle structure*

416        We compare the distribution of scattering heterogeneity with S-wave

417   tomographic models, both because they are the basis for the definition of the Large

418    Low Shear Velocity Provinces, and also show consistency between models [Garnero

419    et al., 2016]. We use several tomographic models: GyPSuM [Simmons et al., 2010],

420    SEMUCB-WM1 [French and Romanowicz, 2014], S40RTS [Ritsema et al., 2011], and

421    TX2011 [Grand, 2002]. Additional comparisons with P-wave models are shown in

422    the supplementary material (Figs. S7-9). We calculate lateral velocity gradients from

423    tomographic models, revealing abrupt changes in mantle structure, which thus

424    serve as a proxy for boundaries of the LLSVPs [Thorne et al., 2004, Garnero et al.,

425    2016]. We calculate gradients over a distance of 10° as the resulting gradients well

426    replicate the margins of the LLSVPs found in forward modelling studies [Garnero et

427    al., 2016 and references therein].

428         We use hotspots from the study of Courtillot et al. [2003]. French and

429    Romanowicz [2015] analysed the tomographic model SEMUCB-WM1 [French and

430    Romanowicz, 2014] and characterised hotspots based on associated tomographic

431    velocity anomalies. We use the 20 hotspots that were labelled as either "primary" or

432    "clear" meaning that the hotspot overlies a column of low velocities from the CMB to

433    1000 km depth with dVs less than -1.5% or less than -0.5 %, respectively.

434         We use slab locations from the Regionalized Upper Mantle (RUM) model,

435    which locates slabs at depth using intra-slab seismicity [Gudmundsson and

436    Sambridge, 1998]. When comparing with scattering heterogeneity locations we use

437    slab locations at the surface (zero depth). Slabs move only a small amount laterally

438    as they subduct (≤5° relative to the plate boundary at the surface [Steinberger et al.,

439    2012]), which is unlikely to strongly influence our correlations.

440        To account for differences in the magnitude, range, and pattern of velocity

441        anomalies and velocity anomaly gradients between tomographic models, and

442        differences in the number of locations in of maps of hotspot and slab locations, we

443        convert maps of tomographic velocities to maps of percentage cumulative area on a

444        sphere sorted by decreasing velocity anomaly (from fast to slow). For example, the

445        20% area corresponds to the area of the 20% highest tomography velocities of a

446        given depth shell (Fig. 6). We only consider the regions of the tomographic models

447        that match the regions sampled by the $P'{\bullet}P'$ dataset at each depth. In this way, the

448        highest and lowest velocities in several tomographic models with inherently

449        differing amplitudes of velocity variation can be directly compared. We establish

450        geographical area percentages associated with the locations of hotspots and

451        subducted slabs by computing the cumulative area surrounding the features within

452        specific distances from them (within the area sampled by the $P'{\bullet}P'$ dataset). For

453        example, the first 20% area for slabs corresponds to the region closest to slabs that

454        adds up to 20% of the Earth's surface area; conversely the last 20% area indicates

455        that amount of surface area furthest from slabs.

456        To estimate correlations between the abundance of small-scale scattering

457        and subducted slabs, hotspots, tomographic velocities and gradients, we compare

458        the location of these features to the distribution of scattering heterogeneity. For

459        each 100 km depth shell, we count scattering heterogeneities in each 20% area

460        division from the feature of interest. To account for the variability in sampling

461        coverage of our dataset (Fig. 3), we count our estimation of potential scatterers

462        (afforded by our event-array distributions) in the same 20% area regions, and

463  calculate the ratio of the number of observed-to-potential heterogeneities. This

464  allows us to construct a map of normalised scattering prevalence, thus effectively

465  removing the bias of our uneven sampling.

466      The first set of comparisons is displayed in Fig. 7 as a cumulative histogram

467  as a function of depth. In the upper 200 km of the mantle, scattering heterogeneities

468  are most common in regions of high velocity (Fig. 7a), which is evident from the

469  horizontal width of the light and dark blue shading being greater than the width of

470  the light and dark red shading over the same depth range. In the lower mantle,

471  especially in the deepest 500 km or so, the opposite is true: scattering

472  heterogeneities are more abundant in low velocity regions (as evident by wider red

473  shading). Regions of the lowermost mantle with high seismic velocities show

474  virtually no correlation with scattering heterogeneities. Scattering is slightly more

475  common in regions of high seismic velocity between 600 and 900 km depth.

476      In the deepest 200 km of the mantle, scattering heterogeneities are more

477  common in regions of high lateral seismic velocity gradients (Fig. 7b: the width of

478  the black and dark blue shading is significantly greater than the light green colors).

479  In the lowest ~1000 km of the mantle, scattering heterogeneities are in greater

480  abundance in the 20% area around hotspots than in any other bin; there is also a

481  slight increase in mapped heterogeneities beneath hotspots in the mid-mantle

482  between 600-900 km depth (see the wide red colors shading, Fig. 7c). Our mapped

483  scattering heterogeneities show little correlation with regions surrounding the

484  surface location of slabs, except in areas furthest from slabs in the 600-900 km

485  depth range (indicated by the wide orange-yellow shading, Fig. 7d). In the upper

486     200 km of the mantle, scattering strongly correlates with high seismic velocities and

487     proximity to slabs (Figs. 7a and 7d, blue and yellow shading, respectively), which, at

488     these shallow depths is most closely related to the location of continents. While the

489     precise locations of the heterogeneities is different, the heterogeneities resolved

490     with P′•P′ show a very similar distribution in the lowermost 300 km of the mantle

491     to those heterogeneities resolved with PK•KP in an earlier study [Frost et al., 2017].

492         To test the robustness of these correlations we determine how likely they are

493     to have been produced by chance. We rotate the tomographic models (of velocity

494     and lateral gradient), and hotspot and slab locations by a random angle about a

495     randomly located pole of rotation. We then recompute the correlations between the

496     rotated geographical features and the distribution of the unrotated scattering

497     heterogeneities. The random rotation is repeated 200 times for each tomography

498     model, as well as for the hotspot and slab locations, to calculate the range of possible

499     correlations. The mean and standard deviation of the range of correlations at each

500     depth is computed, assuming Gaussian statistics. We compare this with the original,

501     unrotated data in Fig. 8, and consider any correlation to be statistically significant if

502     the correlation value between scatterers and regions of the unrotated phenomena

503     plots outside one standard deviation from the mean correlation of the rotated

504     phenomena (demonstrating that at least 84% of the random correlations are a

505     lower value). When we do not assume a distribution and instead calculate the

506     proportion of samples above and below one standard deviation of the data, we find

507     very similar patterns of significant observations. Using this metric, we define the

508     following correlations as significant and unlikely the product of chance:

509     (1) An increased correlation with scatterers in regions of low velocity at depths

510        greater than 1800 km (solid red line in the left panel of Fig. 8a)

511     (2) An increased abundance of scattering heterogeneities in regions of high

512        velocity gradient in the deepest few hundred km of the mantle, as well as

513        between 1600-2000 km depth (solid red line in the right panel of Fig. 8b).

514     (3) An increased abundance of heterogeneities close to surface hotspot locations

515        at depths greater than 2100 km depth (solid red line in left panel of Fig. 8c).

516     (4) A decreased abundance of heterogeneities far from surface hotspot locations

517        at almost all depths greater than 800 km depth (solid red line in right panel

518        of Fig. 8c).

519 There is no significant correlation seen between scatterer locations and slab

520 locations, except an increase in correlation between heterogeneities and large

521 distances from slabs between 600 and 900 km depth, which matches the depth

522 range of the increased correlation with low velocity gradients (solid red lines in

523 left panel of Fig. 8b and right panel of 8d), and an increased correlation between

524 heterogeneities and large distances from slabs throughout much of the lower

525 mantle (which is what one expects if correlations are strong for low velocities).

526

527 *4.2 Dependence upon choice of model*

528       When comparing small-scale scattering locations with tomographically

529 derived high or low velocities, the results may depend upon the choice of the

530 tomography model. In our previous analysis, we compared the distribution of

531 scattering heterogeneities to tomography model SEMUCB-WM1 [French and

532 Romanowicz, 2014]. We further explore the relationship between our mapped fine-

533    scale scattering heterogeneities with large-scale structures in other tomography

534    models: GyPSuM, S40RTS, and TX2011 (Figs. S4-6 and S7-9 for P-wave models). We

535    find small differences in precise depths and magnitudes of correlations with

536    different models, but the correlation between scattering and low velocities at depths

537    below 1600 km, and with high velocities at depths of 200 km and shallower and the

538    robustness of these correlations are consistent between models.

539        To test the dependence of correlation on the pattern of hotspots, in addition

540    to comparing with rotated hotspot locations, we create a population of randomly

541    located hotspots, equal in number to the primary and clear hotspots from Courtillot

542    et al., [2003] and French and Romanowicz [2015]. We find that a synthetic

543    population generates no preferential spatial correlation with the scattering

544    heterogeneities (Fig. S10). Furthermore, when the population of random hotspot

545    locations is rotated to test the robustness of the correlation, the correlation of the

546    random population very often falls well within the one standard deviation range of

547    the rotated data (Fig. S12). This implies that the observed correlation between

548    hotspot locations and scattering heterogeneities in the lower mantle is caused by

549    the specific distribution of hotspots.

550        We test the influence of our decision to use only the surface slab locations of

551    the RUM model. We calculate the spatial correlation between scattering

552    heterogeneities and slab locations as described above, but use slab locations at the

553    depth of the heterogeneity. When considering scattering heterogeneities at depths

554    greater than that which the slab is mapped to we use the location of the slab at the

555    last mapped depth and project this position vertically down to the CMB. This

method of vertical extrapolation likely still misrepresents the locations of slabs: some amount of lateral movement at greater depths is evident in tomographic and geodynamic models but is typically on the order of a few degrees [e.g. French and Romanowicz, 2014 and Steinberger et al., 2012]. Nonetheless, we find no significant difference in the correlations between using the surface slab location and slab locations with depth (Fig. 7 and Figs. S11 and S12).
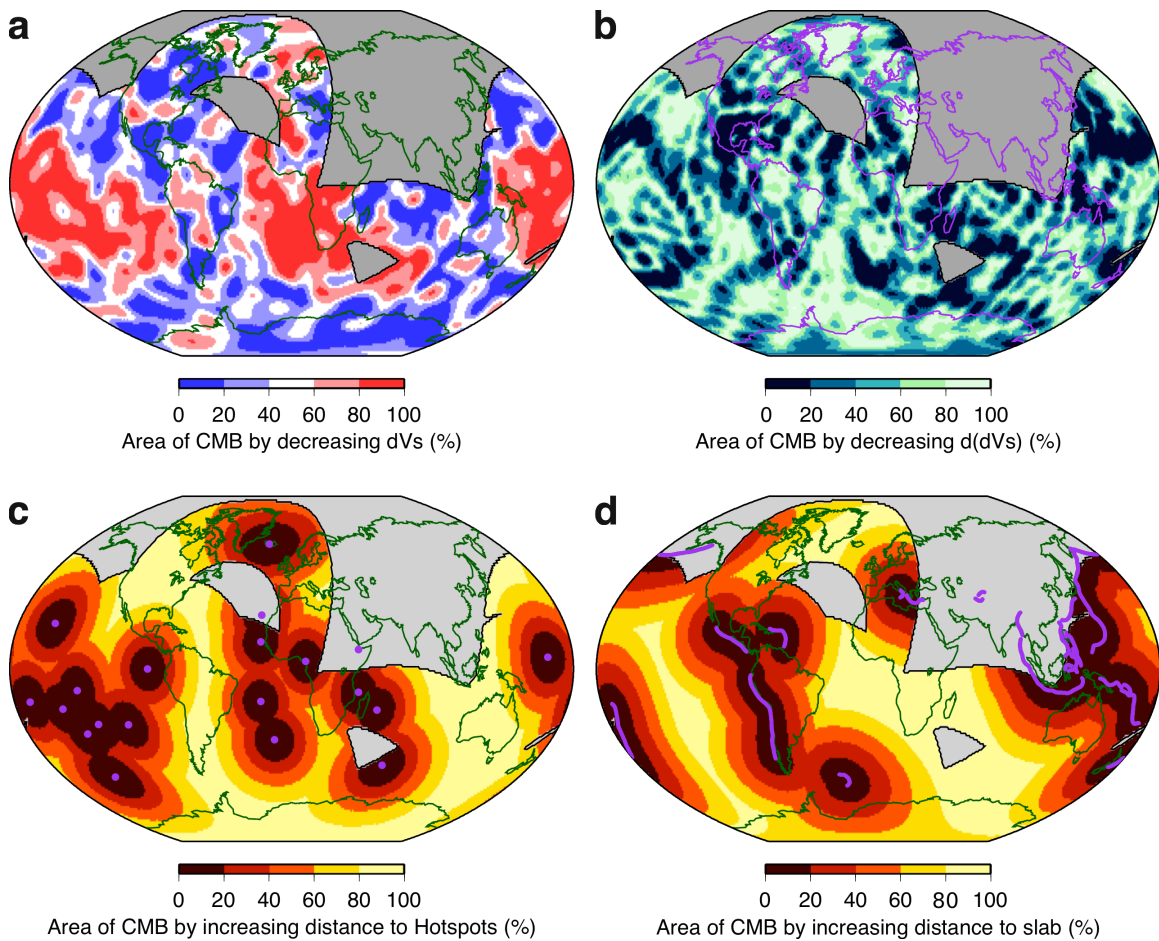


**Figure 6:** Tomography and distance from subduction zones and hotspots by percentage area calculated for sampling at the CMB. (a) The magnitude of the velocity anomalies in SEMUCB-WM1 [French and Romanowicz, 2014] in the area sampled by our dataset at the CMB displayed by decreasing anomaly (from fast blue

568  areas to slow red areas) in regions occupying 20% of the area of the CMB. (b) The

569  magnitude of the lateral velocity gradient decreasing from high to low in 20% area

570  regions. (c) Distance from hotspots (connected to plumes identified as either

571  primary or clear in the analysis of French and Romanowicz [2015]). (d) Distance

572  from slabs (at zero depth slice in RUM [Gudmundsson and Sambridge, 1998]. Black

573  line marks the extent of the sampled area (as in Figure 3d).

574  [2 COLUMN FIGURE]

575

576
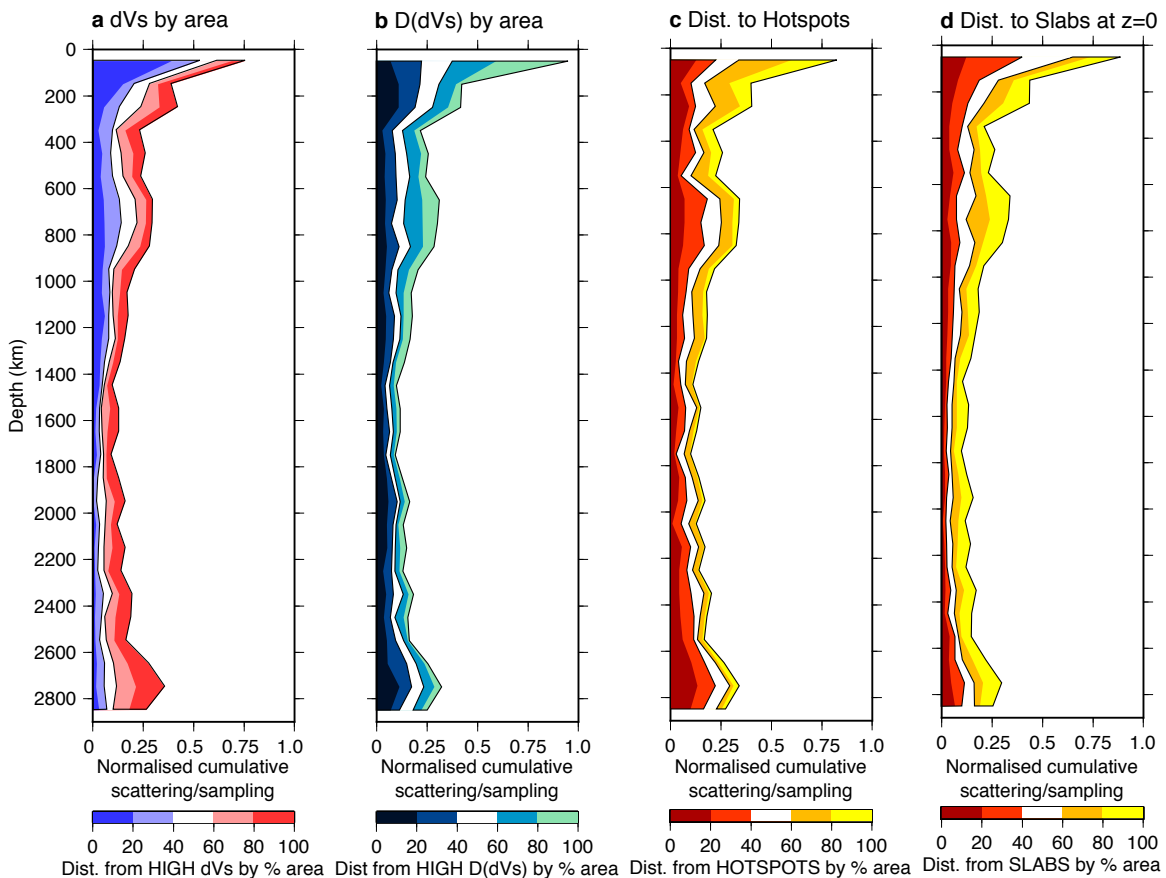


577
578  **Figure 7:** Scattering abundance (bar width) with depth compared with the

579  distribution of large-scale heterogeneity throughout the mantle (colour scale).

580  Scattering abundance is calculated cumulatively across all areas, is divided by

581    sampling, and is normalised to unity, representing the maximum scattering

582    abundance at any depth. **(a)** Scattering heterogeneity and tomographic velocity

583    anomalies (from SEMUCB-WM1 [French and Romanowicz, 2014]) sorted from

584    highest (blue) to lowest (red) measured as a function of surface area in 20% area

585    bins. **(b)** Scattering heterogeneity and lateral tomographic velocity gradient sorted

586    from highest (dark blue) to lowest (light green). **(c)** Scattering heterogeneity and

587    distance from hotspots from low to high (red and yellow, respectively). **(d)**

588    Scattering heterogeneity and distance from slabs from low to high (red and yellow,

589    respectively). Scattering heterogeneity in the lower mantle shows an affinity for

590    both low seismic velocities and hotspots. Black lines encapsulate the highest and

591    lowest 40% area regions.

592    [2 COLUMN FIGURE]

593
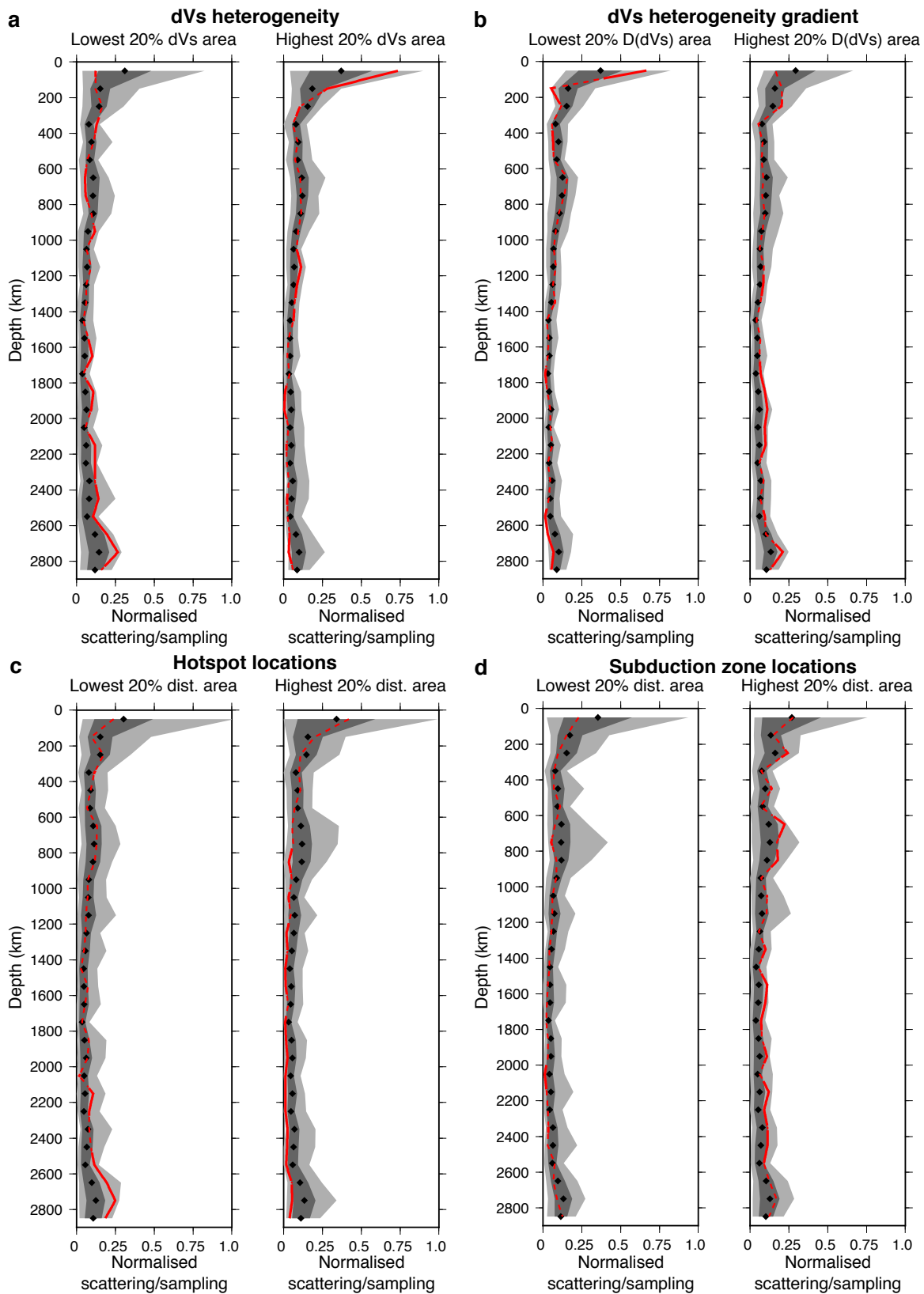
**Figure 8:** Scattering abundance with depth, divided by sampling, showing the unrotated model (red line) compared with rotated models (grey). The unrotated

597    model (red line) is dashed when within one standard deviation (dark gray shading)

598    of the mean of the spatial correlations (black diamonds) with the rotated models,

599    and solid when outside this level. The lighter shaded region marks the range of all

600    correlations with the randomly rotated phenomena. Comparisons are shown for: **(a)**

601    tomographically derived velocity heterogeneity from SEMUCB-WM1 for the 20%

602    area corresponding to the lowest (left panel) and highest velocities (right panel).

603    Correlation between increased scattering abundance and low velocities appears

604    robust in the deepest mantle, and correlation to high velocities is robust in the

605    shallowest 200 km of the mantle, as well as around 1200 km depth. **(b)** As in **(a)**

606    except correlations are between observed scattering and rotated shear velocity

607    gradients in model SEMUCB-WM1. Correlations are most significant for the

608    strongest gradients (right panel) at the base of the mantle. **(c)** As in **(a)** except

609    correlations are between scatterers and distance to rotated hotspot regions.

610    Correlations are most significant in the deepest mantle in close proximity to being

611    beneath hotspots (left panel). **(d)** as in **(c)** except correlations are between

612    scatterers and distance to rotated slab regions. Our random rotation test shows no

613    significant correlation between scatterers and proximity to slabs.

614    [2 COLUMN FIGURE]

615

616
617 **5. Discussion**
618
619        In this study we mapped scattering heterogeneities and explored their

620 geographical relationship to tomographic velocities and gradients, as well as

621 hotspots and slabs.  Our results may be interpreted in terms of the distribution of

622 mantle heterogeneity, which we will discuss here.

623
624 *5.1 Possible origins of scattering heterogeneity in the mantle*
625
626        We observe scattering from small-scale heterogeneity throughout the

627 mantle, with increased heterogeneity at the top and bottom of the mantle. Seismic

628 waves can be scattered by volumetric heterogeneity with sharp impedance

629 contrasts, when the heterogeneity has a minimum scale length comparable to the

630 wavelength of the incident wave. Our method is not capable of resolving the precise

631 partitioning of the incident wavefield into scattered versus transmitted energy,

632 since we do not have a consistent reference phase to compare to the amplitude of

633 the scattered wave. Thus we are unable to constrain the properties of the

634 heterogeneities (e.g. impedance contrast). Nonetheless, the frequencies of waves

635 that we study (between 0.5 and 2.0 Hz) imply that observed scattering

636 heterogeneities have a minimum scale length of one to tens of km.

637        A variety of structures could scatter the energy observed in our data. We can

638 use the distribution and sizes of scattering heterogeneities to address the feasibility

639 of possible causes. Material undergoing phase changes such as from bridgmanite to

640 post-perovskite (pPv) in the lower mantle (or the back transformation) [Murakami

641 et al., 2004; Oganov and Ono, 2004], as well as transitions of olivine to wadsleyite to

642    ringwoodite to perovskite through the upper mantle transition zone could provide

643    an impedance contrast with the ambient mantle. The bridgmanite to pPv phase

644    transition is predicted to occur in the deepest few 100 km of the mantle, and only in

645    relatively cold regions of the mantle for a standard pyrolitic composition, thus

646    would not be appropriate to explain scattering at all depths and locations, unless

647    mineralogical alterations are considered [Lay et al. 2006]. The phase transition is

648    controlled by temperature, composition, and pressure. While pressure is assumed

649    hydrostatic, local changes in composition, perhaps by contamination of the mantle

650    by subducted mid-ocean ridge basalt (MORB), may influence the pPv transition

651    [Grocholski et al., 2012], possibly causing the transition to occur locally in the

652    vicinity of the MORB contamination. Metastability of phase transitions due to

653    chemical heterogeneity [Catalli et al., 2009] could allow transformed minerals to

654    persist outside of their expected stability range. High thermal conductivity in the

655    lower mantle [Stackhouse et al., 2015] renders small-scale temperature changes an

656    unlikely cause of spatially limited occurrence of the pPv transition. While many

657    morphologies and scale lengths of pPv regions can be envisioned that could

658    contribute to wave field scattering observed here, the details of such processes are

659    not constrained. However, pPv should not be stable in the upper mantle, and thus

660    cannot explain observed scattering there. Nonetheless, pPv remains a viable

661    contributor to wavefield scattering in the deepest mantle.

662        The subduction process continuously introduces compositional

663    heterogeneity into the mantle. Scattering has previously been mapped in the upper

664    mantle and lower mantle in the proximity of subduction zones [Kaneshima and

665    Helffrich, 1998; Rost and Earle, 2010; Miller and Niu, 2008; Bentham and Rost,

666    2014]. We do not observe a robust preference of scattering heterogeneity in upper

667    mantle regions of subduction over other regions. While we do observe slightly

668    increased scattering in regions associated with subduction at around 600 to 900 km

669    depth (Fig. 7a), this does not appear to be statistically significant (Fig. 8a, right

670    panel). Nonetheless, the increased concentration of scattering heterogeneity

671    between 600 and 900 km depth shows robust spatial correlation with regions away

672    from subduction zones and areas of low amplitude lateral velocity gradient (Figs. 7

673    and 7). In some tomographic models subducting slabs are observed to flatten at a

674    similar depth, between ~800-1200 km depth [e.g. French and Romanowicz, 2015].

675        Oceanic crust may be responsible for scattering throughout the mantle.

676    Subducted oceanic crust may remain unmixed due to slow chemical diffusion rates

677    [Olson et al., 1984] and is only homogenised into the mantle through mechanical

678    stirring. If the observed scattering heterogeneities are oceanic crust then the

679    dispersal of heterogeneities throughout the mantle must be faster than stirring and

680    removal of heterogeneities since scattering heterogeneity is also observed in

681    regions that have not been influenced by subduction for a long time.

682        The iron spin transition affects the velocity and density of iron-bearing

683    mantle materials [Lin et al., 2005]. Recently, this has been observed to occur over a

684    60 GPa pressure range (~600 to 2000 km depth) [Holmstrom and Stixrude, 2015]

685    and thus would likely not generate discrete heterogeneities capable of causing

686    scattering.

687      Products of chemical reactions between core and mantle materials are

688      predicted to have physical properties in contrast with the ambient mantle [Knittle

689      and Jeanloz, 1989] thus may be capable of causing seismic scattering. Experiments

690      demonstrate that such mantle material enriched in iron would likely be denser than

691      the ambient mantle [Wicks et al., 2010]. An interesting possibility is the

692      development of a reaction product layer that would inhibit further interaction with

693      the core; for this case, products are likely to be constrained to a very limited

694      thickness close to the CMB, on the order of a few meters to kilometers [Kanda and

695      Stevenson, 2006]. However, flow in the deep mantle could generate thicker

696      accumulations of reaction products [Mao et al., 2006], which could scatter waves.  In

697      addition, ULVZs are commonly imaged to have vastly reduced seismic velocities of

698      up to -10% dVp and -30% dVs, and increased density of +10-20% relative to the

699      surrounding mantle [e.g., McNamara et al., 2010]. Partial melt of mantle material has

700      been proposed as an explanation of ULVZs [Williams and Garnero, 1996]. Partial

701      melt may be denser than the solid state [Ohtani and Maeda, 2001] as well as having

702      strongly reduced seismic velocities. While ULVZs and CMB reaction products could

703      explain deeper scattering heterogeneities, simulations have suggested that dense

704      material may also be entrained up to 200 km above the CMB, dependent on density,

705      viscosity, and vigor of mantle flow [Bower et al., 2011]. CMB topography or

706      roughness might cause scattering [Chang and Cleary, 1981; Mancinelli et al., 2016],

707      but this could not explain heterogeneities we map up off of the CMB throughout the

708      mantle. LLSVPs may be compositionally distinct from the surrounding mantle [e.g.

709      Garnero et al., 2016], and dynamical flow models predict that the LLSVP material

710 will be gradually entrained into mantle flow on small length scales [Li et al., 2014;

711 Williams et al., 2015; Mulyukova et al., 2015]. Thus, depending on the LLSVP

712 properties and entrained heterogeneity scale, this process might give rise to

713 scattering. Geodynamic models also predict that surrounding ambient mantle

714 material can be downward entrained into the LLSVPs, thus offering an origin of

715 scattering within LLSVP regions.

716
717 *5.2 Distribution of scattering heterogeneity*
718
719   The distribution of small-scale volumetric heterogeneities is likely strongly

720 dependent on the dynamic properties and processes within the Earth. In numerical

721 simulations of mantle dynamics small-scale heterogeneity, particularly that derived

722 from subducted oceanic crust, tends to be concentrated in regions of upwelling from

723 the lower mantle around plumes and downwelling from the surface around

724 subduction zones (Fig. 1 of Li et al., [2014]). The same focusing beneath upwellings

725 is expected for basal heterogeneities [McNamara et al., 2010] (e.g., compositionally

726 distinct ULVZ material, CMB reaction products, and entrained LLSVP material).

727 Furthermore, large-scale mantle heterogeneity may influence radial small-scale

728 heterogeneity distribution by modifying the convective flows in which the

729 heterogeneities could be entrained [Li et al., 2014].

730   As wavelength at some fixed frequency is a function of the local velocity,

731 which changes with depth, and the wavelength of scattering structure that can be

732 resolved is dependent on the incident frequency, it follows that in band limited data,

733 the resolvable scattering wavelength changes with depth. We filter all data between

734 0.5 and 2.0 Hz, therefore, we resolve scattering heterogeneity with wavelengths

735 between about 7-28 km at the CMB, decreasing to about 3-12 km at the surface.

736 Stirring of initially larger-scale heterogeneity is suggested to lead to a cascade of

737 heterogeneity sizes, increasing in abundance with decreasing scale [Olson et al.,

738 1984]. A previous study of the scale of scattering heterogeneities in the lowermost

739 mantle found the most common scale-length to be 4-7 km, but other scales were

740 also present [Frost et al., 2017]. Despite the limited frequency range used in this

741 study, we are likely imaging heterogeneity of a similar size (around 7 km)

742 throughout the mantle.

743       The similarity between scattering heterogeneity abundance and tomographic

744 amplitude (Fig. 5) may arise from processes relating to convection and chemical

745 differentiation that likely generate strong lateral velocity variations on continental

746 scales and smaller through stirring and diffusion. Lower mantle anomalies manifest

747 at a range of spatial scales (LLSVPs, ULVZs, D′′, CMB reaction products), and stirring

748 and entrainment may further decrease their size [Olson et al., 1984, Li et al., 2014],

749 leading both to high-amplitude large-scale velocity anomalies and abundant small-

750 scale scattering. Upper mantle heterogeneity related to subduction, magmatism, and

751 convective processes are also likely to occur across scales.  In addition to increased

752 scattering at the top and bottom of the mantle, we also observe a slight but marked

753 increase in scattering abundance from 600-900 km depth, independent of the

754 tomographic velocity structure, which may relate to slab subduction processes or

755 large-scale vertical viscosity changes [Rudolph et al., 2015].

756
757 **6. Conclusion**
758

759        Through analysis of the high-frequency seismic wavefield we map the

760        distribution of small-scale seismic heterogeneity, on the order of ∼1-10 km in size,

761        throughout Earth's mantle. We deterministically locate vastly more scattering

762        heterogeneities than has been done previously, significantly improving our

763        understanding of small-scale mantle structure. The spatial distribution and scale-

764        length of this scattering heterogeneity suggests it may be the product of several on-

765        going processes in the mantle. These include oceanic crust disseminated throughout

766        the mantle, entrainment of basal heterogeneities such as ULVZ material or core-

767        mantle reaction product, and compositionally distinct LLSVP material swept into

768        mantle flow. Subducted MORB may suitably explain all scattering observations

769        without scattering contributions from other sources. However, we cannot rule out

770        that scattering is caused by a mixture of heterogeneities with different origins in

771        different regions and depths. While small-scale heterogeneity appears present in

772        much of the mantle, we find increased scattering heterogeneity within the

773        uppermost 200 km of the mantle and the lowermost 300 km of the mantle, similar

774        to heterogeneity amplitudes seen in tomography models. We find no statistically

775        significant correlation between scattering and subducting slabs in the upper 1000

776        km of the mantle. In the lower mantle (from around 1500 km depth down to the

777        CMB), scattering is most common in regions related to the LLSVPs and close to

778        deeply sourced mantle hotspots. Meanwhile, scattering is rare in regions far from

779        deeply sourced mantle hotspots. This suggests that large-scale convective lower

780        mantle structures may entrain and concentrate small-scale heterogeneity in regions

781        of upwelling, downwelling, and stagnant flow.

789

790

791

792  **References:**
793  Bentham, H. L. M. & Rost, S. Scattering beneath Western Pacific subduction zones:
794  evidence for oceanic crust in the midmantle. Geophysical Journal International 197,
795  1627–1641 (2014).
796
797  Blandford, R. R. An automatic event detector at the Tonto Forest seismic
798  observatory. Geophysics 39, 633–643 (1974).
799
800  Bower, D. J.,Wicks,J.K.,Gurnis,M. & Jackson, J. M.A geodynamic and mineral physics
801  model of a solid-state ultralow-velocity zone.Earth Planet. Sci. Lett. 303,193–202
802  (2011).
803
804  Bondar, I., North, R.G., Beall, G., 1999. Teleseismic slowness-azimuth station correc-
805  tions for the International Monitoring System seismic network. Bull. Seism. Soc.
806  Am.89, 989–1003.
807
808  Brandenburg, J. P. & van Keken, P. E. Deep storage of oceanic crust in a vigorously
809  convecting mantle. Journal of Geophysical Research 112, 1–15 (2007).
810
811  Capon, J., Greenfield, R. & Kolker, R. Multidimensional maximum-likelihood
812  processing of a large aperture seismic array. Proc. IEEE 55, 192–211 (1967).
813
814  Catalli, K., Shim, S.-H. & Prakapenka, V. Thickness and Clapeyron slope of the post-
815  perovskite boundary. Nature 462, 782–5 (2009).
816
817  Chang, A. C. & Cleary, J. R. Scattered PKKP: Futher evidence for scattering at a rough
818  core-mantle boundary. Phys. Earth planet. Int. 24, 15–29 (1981).

819
820 Cleary, J. & Haddon, R. A. W. Seismic wave scattering near the core-mantle
821 boundary: a new interpretation of precursors to PKP. Nature 240, 549–551 (1972).
822
823 Courtillot, V., Davaille, A., Besse, J. & Stock, J. Three distinct types of hotspots in the
824 Earth's mantle. Earth Planet. Sci. Lett. 205, 295–308 (2003).
825
826 Domeier, M., Doubrovine, P. V., Torsvik, T. H., Spakman, W. & Bull, A. L. Global
827 correlation of lower mantle structure and past subduction. Geophys. Res. Lett.
828 4945–4953 (2016).
829
830 Doubrovine, P. V., Steinberger, B. & Torsvik, T. H. A failure to reject: Testing the
831 correlation between large igenous provinces and deep mantle structures with EDF
832 statistics. Geochem. Geophys. Geosyst. 1130–1163 (2016).
833
834 French, S. W. & Romanowicz, B. A. Whole-mantle radially anisotropic shear-
835 velocity structure from spectral-element wave form tomography. Geophys. J. Int.199,
836 1303–1327 (2014).
837
838 French, S. W. & Romanowicz, B. A. Broad plumes rooted at the base of the Earth's
839 mantle beneath major hotspots. Nature 525, 95–99 (2015).
840
841 Frost, D. A., Rost, S., Selby, N. D. & Stuart, G. W. Detection of a tall ridge at the core-
842 mantle boundary from scattered PKP energy. Geophys. J. Int. 195, 558–574 (2013).
843
844 Frost, D. A., Rost, S., Garnero, E. J. & Li, M. Seismic evidence for Earth's crusty deep
845 mantle. Earth and Planetary Science Letters 470, 54–63 (2017).
846
847 Garnero, E. J., McNamara, A. K. & Shim, S.-h. Continent-sized anomalous zones with
848 low seismic velocity at the base of Earth's mantle. Nature Geosci. 1–9 (2016).
849
850 Grand, S. P. Mantle shear-wave tomography and the fate of subducted slabs. Phil.
851 Trans. R. Soc. Lond A 360, 2475–2491 (2002).
852
853 Grocholski, B., Catalli, K., Shim, S.-H. & Prakapenka, V. Mineralogical effects on the
854 detectability of the postperovskite boundary. Proceedings of the National Academy
855 of Sciences 109, 2275–2279 (2012).
856
857 Gudmundsson, O. & Sambridge, M. A regionalized upper mantle (RUM) seismic
858 model. J. Geophys. Res. 103, 7121–7136 (1998).
859
860 Hedlin, M. A. H., Shearer, P. M. & Earle, P. S. Seismic evidence for small-scale
861 heterogeneity throughout the Earth's mantle. Nature 387, 145–150 (1997).
862
863 Holmström, E. & Stixrude, L. Spin Crossover in Ferropericlase from First-Principles
864 Molecular Dynamics. Phys. Rev. Lett. 117202, 1–5 (2015).

865

866 Kanda, R. V. S. & Stevenson, D. J. Suction mechanism for iron entrainment into the
867 lower mantle. Geophys. Res. Lett. 33, 4–7 (2006).

868

869 Kaneshima, S. & Helffrich, G. Detection of lower mantle scatterers northeast of the
870 Marianna subduction zone using short-period array data. J. Geophys. Res. 103,
871 4825–4838 (1998).

872

873 Knittle, E. & Jeanloz, R. Simulating the core-mantle boundary: An experimental study
874 of high pressure reactions between silicates and liquid iron. Geophys. Res. Lett. 16,
875 609–612 (1989).

876

877 Lay, T., Hernlund, J., Garnero, E. J. & Thorne, M. S. A post-perovskite lens and D" heat
878 flux beneath the central Pacific. Science 314, 1272–6 (2006).

879

880 Li, M., McNamara, A. K. & Garnero, E. J. Chemical complexity of hotspots caused by
881 cycling oceanic crust through mantle reservoirs. Nature Geosci. 7, 366–370 (2014).

882

883 Lin, J-f., Struzhkin, V. V., Jacobsen, S. D., Hu, M. Y., Chow, P., Kung, J., Liu, H., Mao, H-k.
884 & Hemley, R. J.. Spin transition of iron in magnesiowustite in the Earth's lower
885 mantle. Nature 436, 377–380 (2005).

886

887 Mancinelli, N. J. & Shearer, P. M. Reconciling discrepancies among estimates of small-
888 scale mantle heterogeneity from PKP precursors. Geophys. J. Int. 195, 1721–1729
889 (2013).

890

891 Mancinelli, N., Shearer, P. & Thomas, C. On the frequency dependence and spatial
892 coherence of PKP precursor amplitudes. J. Geophys. Res. 121, 1873–1889 (2016).

893

894 Mao, W. L. et al. Iron-rich post-perovskite and the origin of ultralow-velocity zones.
895 Science 312, 564–5 (2006).

896

897 McNamara, A. K. & Zhong, S. Thermochemical structures beneath Africa and the
898 Pacific Ocean. Nature 437, 1136–9 (2005).

899

900 McNamara, A. K., Garnero, E. J. & Rost, S. Tracking deep mantle reservoirs with ultra-
901 low velocity zones. Earth Planet. Sci. Lett. 299, 1–9 (2010).

902

903 Miller, M. & Niu, F. Bulldozing the core mantle boundary: Localized seismic
904 scatterers beneath the Caribbean Sea. Phys. Earth planet. Int. 170, 89–94 (2008).

905

906 Mulyukova, E., Steinberger, B., Dabrowski, M. & Sobolev, S. V. Survival of LLSVPs for
907 Billions of Years in a Vigorously Convecting Mantle: Replenishment and Destruction
908 of Chemical Anomaly. J. Geophys. 3824–3847 (2015).

909

910  Murakami, M., Hirose, K., Kawamura, K., Sata, N. & Ohishi, Y. Post-perovskite phase
911  transition in MgSiO3. Science 304, 855–858 (2004).
912
913  Oganov, A. R. & Ono, S. Theoretical and experimental evidence for a post-perovskite
914  phase of MgSiO3 in Earth's D" layer. Nature 430, 445–448 (2004).
915
916  Ohtani, E. & Maeda, M. Density of basaltic melt at high pressure and stability of the
917  melt at the base of the lower mantle. Earth Planet. Sci. Lett. 193, 69–75 (2001).
918
919  Olson, P., Yuen, D. A. & Balsiger, D. Mixing of passive heterogeneities by mantle
920  convection. J. geophys. Res. 89, 425–436 (1984).
921
922  Ritsema, J., Deuss, A. F., van Heijst, H. J. & Woodhouse, J. H. S40RTS: a degree-40
923  shear-velocity model for the mantle from new Rayleigh wave dispersion, teleseismic
924  traveltime and normal-mode splitting function measurements. Geophys. J. Int. 184,
925  1223–1236 (2011).
926
927  Rost, S. & Earle, P. S. Identifying regions of strong scattering at the coremantle
928  boundary from analysis of PKKP precursor energy. Earth Planet. Sci. Lett. 297, 616–
929  626 (2010).
930
931  Rost, S., Earle, P. S., Shearer, P. M., Frost, D. A. & Selby, N. D. Seismic detections of
932  small-scale heterogeneities in the deep Earth. In Khan, A. & Deschamps, F. (eds.) The
933  Earth's Heterogeneous Mantle, chap. 12, 367–390 (Springer International
934  Publishing, 2015).
935
936  Rudolph, M. L., Lekic, V. & Lithgow-Bertelloni, C. Viscosity jump in Earth's mid-
937  mantle. Science 350, 1349–1352 (2015).
938
939  Selby, N. D. Improved Teleseismic Signal Detection at Small-Aperture Arrays. Bull.
940  seism. Soc. Am. 101, 1563–1575 (2011).
941
942  Simmons, N. A., Forte, A. M. & Grand, S. P. Joint seismic, geodynamic and mineral
943  physical constraints on three-dimensional mantle heterogeneity: Implications for
944  the relative importance of thermal versus compositional heterogeneity. Geophysical
945  Journal International 177, 1284–1304 (2009).
946
947  Stackhouse, S., Stixrude, L. & Karki, B. B. First-principles calculations of the lattice
948  thermal conductivity of the lower mantle. Earth Planet. Sci. Lett., 427, 11-17 (2015).
949
950  Steinberger, B., Torsvik, T. H. & Becker, T. W. Subduction to the lower mantle a
951  comparison between geodynamic and tomographic models. Solid Earth 3, 415-432
952  (2012).
953
954  Tackley, P. J. Mantle Geochemical Geodynamics. In Treatise on Geophysics, chap.
955  7.12, 521–585 (Elsevier B.V., 2015), 2nd edn. edn.

956

957 Thomas, C., Weber, M., Wicks, C. W. & Scherbaum, F. Small scatterers in the lower
958 mantle observed at German broadband arrays. J. Geophys. Res. 104, 15073–15088
959 (1999).

960

961 Thorne, M., Garnero, E. J. & Grand, S. P. Geographic correlation between hot spots
962 and deep mantle lateral shear-wave velocity gradients. Phys. Earth Planet. Int. 146,
963 47–63 (2004).

964

965 Waszek, L., Thomas, C. & Deuss, A. PKP precursors : Implications for global
966 scatterers. Geophys. Res. Lett. (2015).

967

968 Wen, L. Intense seismic scattering near the Earth's core-mantle boundary beneath
969 the Comoros hotspot. Geophys. Res. Lett. 27, 3627–3630 (2000).

970

971 Wicks, J. K.,Jackson,J.M. & Sturhahn, W. Very low sound velocities in iron-rich
972 (Mg,Fe)O: Implications for the core-mantle boundary region. Geophys. Res. Lett. 37,
973 1–5 (2010).

974

975 Williams, C. D., Li, M., Mcnamara, A. K., Garnero, E. J. & Soest, M. C. V. Episodic
976 entrainment of deep primordial mantle material into ocean island basalts. Nat.
977 Commun. 6, 1–7 (2015).

978

979 Williams, Q. & Garnero, E. J. Seismic Evidence for Partial Melt at the Base of Earth's
980 Mantle. Science 273, 1528–1530 (1996).

981

982 Yao, J. & Wen, L. Seismic structure and ultra-low velocity zones at the base of the
983 Earth's mantle beneath Southeast Asia. Physics of the Earth and Planetary Interiors
984 233, 103–111 (2014).

985
986
987